AEROTHERMAL ANALYSIS OF THE RETPRO FLIGHT CONFIGURATION

*M. Laureti *, S. Karl *, T. Bykerk * and D. Kirchheck ***

* DLR Institute of Aerodynamics and Flow Technology
Bunsenstr. 10, 37073 Göttingen, Germany
mariasole.laureti@dlr.de - sebastian.karl@dlr.de - tamas.bykerk@dlr.de

** DLR Institute of Aerodynamics and Flow Technology,
Supersonic and Hypersonic Technologies Department
Linder Höhe, 51147 Cologne, Germany
daniel.kirchheck@dlr.de

ABSTRACT

The RETPRO (Validation of Wind Tunnel Test and CFD Techniques for Retro-propulsion) project, part of ESA´s Future Launchers Preparatory Programme (FLPP), aims to investigate launch system reusability technologies using wind tunnel testing and computational fluid dynamics (CFD). This paper describes and summarizes the CFD based aerothermal load predictions for a Vertical Take-off Vertical Landing (VTVL) reusable launcher configuration during the retro-propulsion phase. An analysis of representative numerical results, obtained for the case Mach 5.3 and three active engines, is provided with the aim to show typical flow field phenomena and the resulting heating patterns occurring on the launcher surface. Parametric studies are performed to evaluate the effect of the number of operating engines, thrust vector control and different fuels (hydrocarbon vs. hydrogen).

Index Terms— Reusable Launch Vehicle, Retro-Propulsion, Aerothermal Loads, CFD, RANS

1. INTRODUCTION

In the ever-evolving landscape of space exploration, the quest for efficiency, sustainability and cost effectiveness has led to a paradigm shift towards reusable space launch systems. Within Europe, a confluence of ambitious programs and initiatives, led by both government agencies and private companies, is driving the advancement of reusable space launchers.

At the forefront of European efforts to address these challenges is the European Space Agency (ESA), which has been instrumental in fostering collaboration and innovation across the state members. Through initiatives such as the Future Launchers Preparatory Programme (FLPP), ESA aims at developing the necessary know-how for future launch systems to be able to guarantee Europe's needs for a secured and autonomous access to space. Part of the strategy consists in promoting the development of cutting-edge technologies for Vertical Take-off Vertical Landing (VTVL) Reusable Launch Vehicles (RLVs) and concepts for next-generation launch systems.

The European knowledge and expertise in that field is growing thanks to systematic studies on possible future European launchers [1, 2] and detailed investigations of system components, a notable example is the Horizon 2020 RETALT project [3]. A valuable contribution to the research and development of reusable launchers has been made also by CALLISTO (Cooperative Action Leading to Launcher Innovation in Stage Toss back Operations) project, born from the collaboration between DLR, CNES and JAXA [4, 5].

Nonetheless, numerical and experimental tools are not yet validated completely for the full range of a commercially relevant launcher trajectory, including high altitude control and propulsive maneuvers, as well as advanced aerodynamic control surfaces, like grid fins.

The RETPRO (Validation of Wind Tunnel Test and CFD Techniques for Retro-propulsion) project, part of ESA's FLPP, aims to prepare and validate the necessary tools for reliable design and simulation of a descent trajectory of a proposed in-line VTVL launcher configuration using retro-propulsion and aerodynamic surface control to perform entry, descent and landing maneuvers. Tools required for preliminary aerodynamic design include wind tunnel testing (WTT) and computational fluid dynamics (CFD) to generate a comprehensive aerodynamic/aerothermal database (AEDB/ATDB) needed for flight dynamics simulations to enable mission and performance analysis of possible future launcher designs [6].

One of the major differences between conventional and reusable launch vehicles is the retro burn maneuver, which presents new aerodynamic and aerothermodynamic challenges due to the interaction of the engine plume with the launcher structure, resulting in changes in aerodynamic behavior, increased heat flux, and possibly even deposition of

exhaust gases. The assessment of thermal loads occurring on reusable launch vehicles is essential for ensuring the correct sizing of the thermal protection system as well as other important structural parts like aerodynamic control surfaces, i.e. planar fins/grid fins, and landing legs.

Due to the extremely high cost and reduced diagnostic capability associated with flight test campaigns and the limitations of wind tunnel testing due to complex scaling for flight configuration, the evaluation of thermal loads experienced by reusable launch vehicles throughout the trajectory is primarily based on numerical simulations [7, 8, 9, 10, 11, 12, 13]. CFD can overcome limitations of experiments, such as: simulating accurate flight conditions (Reynolds number, ambient pressure, etc.), using correct O/F ratios for plume simulation and modeling complicated features such as gas generators. On the other hand, ground tests are essential for the validation of numerical models.

This work analyses the results of representative CFD simulations highlighting the presence of typical flow field phenomena that occur during the descent trajectory, with a focus on the re-entry burn, and the resulting heating pattern on the rocket structure. Interesting phenomena affecting the aerothermodynamic heating of the vehicle surface are represented by plume spreading, plume-to-plume interactions and vehicle immersion in hot exhaust gases. Parametric studies are performed to evaluate the effect of the number of operating engines, thrust vector control and different fuels (hydrocarbon vs. hydrogen).

Steady-state RANS simulations are performed with the DLR-TAU code on the RETPRO VTVL configuration. The flight profiles of the candidate reference missions have been reconstructed based on existing missions selected in Ref. [6].

2. VTVL FLIGHT CONFIGURATION LAYOUT & MISSION

The underlying geometry used for the CFD calculations is shown in figure 1. It is a generic representation of a VTVL reusable launch system, including grid fins, landing legs, and a simplified base geometry. The properties of this reference configuration can be found in Ref. [6].

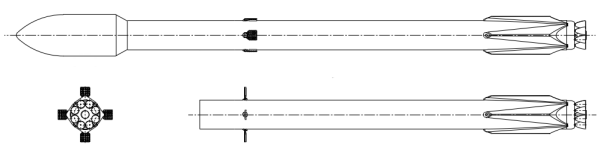

Fig. 1: Shape of the generic reference launcher configuration [6]

Trajectory reference data is taken from existing webcasts from flown commercial launchers. The reference taken is designed to launch satellites into Low Earth Orbit (LEO) or Geostationary Transfer Orbit (GTO). In the former case, the first stage booster lands after a Return to Launch Site (RTLS) near the launch pad, while in the latter case, the booster lands as a Downrange Landing (DRL) on an offshore platform at a specified downrange distance. Typical flight profiles are depicted in figure 2.

The CFD matrix has been set to be consistent with the experimental matrix to allow ground-to-flight extrapolation and includes characteristic points for both flight profiles as well as points outside of them (academic interest).

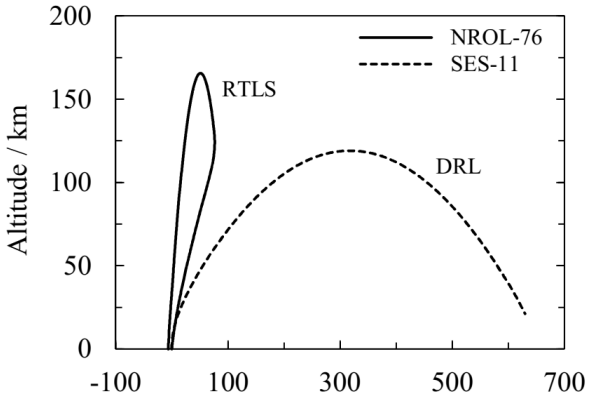

Fig. 2: Flight profiles taken from flown commercial launchers webcast [6]

3. MATHEMATICAL & NUMERICAL MODEL

The CFD simulations were performed with the DLR-TAU code, which is a second-order finite-volume solver for the Euler and Navier-Stokes equations, including a comprehensive set of RANS-based or scale-resolving turbulence models and extensions for chemically reacting high-enthalpy flows. [14]. It uses unstructured computational grids to facilitate the analysis of complex geometries and is highly optimized for the application on massively parallel HPC systems. TAU has been successfully applied to a wide range of sub- to hypersonic flow problems, both in scientific and industrial applications, including the analysis of re-usable launcher configurations.

The baseline set of numerical models which have been applied for the present investigations provides accurate and robust treatment for all flow conditions as defined in the CFD test matrix with free stream Mach numbers ranging from 0.5 to 7. The calculation of the inviscid fluxes in the finite volume framework is based on the application of the AUSMDV flux vector splitting scheme together with MUSCL gradient reconstruction to achieve second order spatial accuracy. Viscous fluxes are treated with a low-dissipation central discretization scheme.

Turbulence was modeled with a Spalart-Allmaras one-equation RANS model in low Reynolds formulation [15]. This model provides a good compromise between numeri-

cal efficiency and accuracy and is particularly applicable to flows with strong compression shocks. It has been shown in previous studies [16] that the RANS plume structure of a Spalart-Allmaras-Model compares well to LES reference data.

The estimates of surface heat flux are based on isothermal walls with a constant temperature of 300K.

Nozzle exhaust, where applicable, was modeled by imposing the exit flow conditions of the thrust nozzles at their respective exit planes in the computational domain of the launcher. The radial distribution of the axial and radial velocity, exit pressure and temperature was determined by separate analyses of the flow inside the thrust nozzle, which provides an accurate representation of the exhaust jets in the three dimensional computations.

The thermo-chemical modeling is generally based on a reacting mixture of thermally perfect gases and the solution of a transport equation for each component. The properties of the individual species are either computed from spectroscopic constants using partition functions that include an accurate representation of high temperature effects such as anharmonic-corrections and coupling of rotational and vibrational degrees of freedoms for molecules [17] or from NASA-Polynomials [18]. Appropriate mixture rules are applied to compute the thermodynamic properties depending on the local gas composition, pressure and density. Species viscosities are computed from Blottner or Sutherland curve fits. Heat conductivity is estimated from the Eucken-correction. Turbulent heat conductivity is obtained from a constant ratio of laminar to turbulent Prandtl numbers of 0.8. The turbulent diffusivity is calculated using a constant turbulent Schmidt number of 0.7.

The free stream air was modeled as a mixture of 76% N2 and 24% O2 by mass fraction. The composition of the engine exhaust was prescribed at the nozzle exit planes as radially distributed partial densites of the major exhaust species from separate nozzle flow analyses (section 5). The additional heat release due to post-combustion of the fuel-rich exhaust gases in the flow field around the rocket configuration was neglected for hydrogen fueled configurations which is justified by preparatory studies (section 6). For Kerosene, a global 3-step mechanism [19] was employed.

4. MODEL GEOMETRY AND GRID GENERATION

The basic external shape was defined by the RETPRO flight configuration as provided by the system studies. The overall length of the configuration is 47m (without nozzles) with a diameter 3.66m. The significant size of the rocket results in large Re-numbers during flight phases with high dynamic pressure associated with thin boundary layers, which need thin prismatic mesh layers in the computational grid. During high altitude flight and retro-maneuvers, boundary layers are much thicker. Hence grids with different boundary layer resolutions were generated to ensure accurate resolution and computational efficiency. Generally, the prismatic sub-layers close to the wall were constructed to ensure a first dimensionless wall spacing of y^+ in the order of one and a wall normal stretching ratio of grid cells of less than 1.3. A quarter computational domain was used as a baseline. For the cases with angle of attack and thrust vector control a half configuration was used.

Surface meshing used a hybrid approach. Unstructured triangular meshes were applied to complex features such as landing legs or grid fins. Smooth regions on the surface were meshed with structured quadrilateral meshes which slightly improves the accuracy of the flow solver due to the availability of line detection algorithms for gradient reconstruction.

The overall sizes of the computational grids were around 16M and 32M points for the quarter and half configurations, respectively.

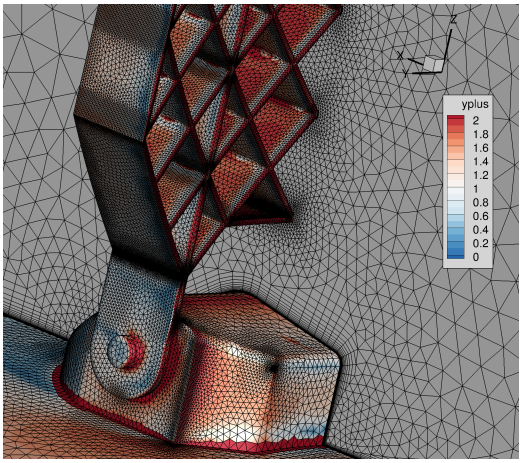

(a) grid fin

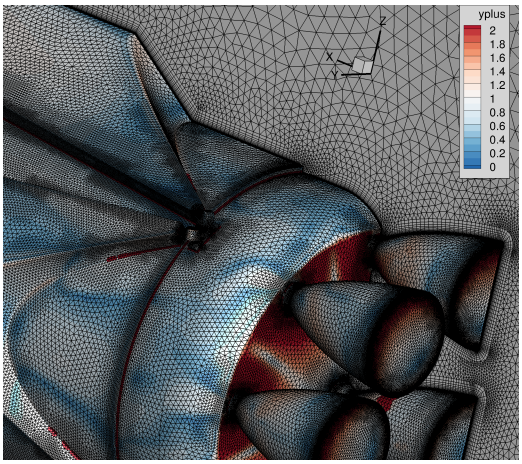

(b) base region

Fig. 3: Computational grid details

Some features of the computational grid are shown in figure 3. The surface is colored with the y^+ distribution of the first prismatic layer for the most critical conditions for y^+. These conditions correspond to the aerodynamic (plume-off) case with the peak Reynolds number along the trajectory (free stream: Mach = 1.4, p = 85kPa). Base-plate and grid fins contain the regions of peak y^+ values.

5. INTERNAL FLOW PATH ANALYSIS

The CFD analyses of the RETPRO flight configurations require an accurate representation of the exhaust plumes of the rocket engines. The thrust nozzles operate in full-flowing mode at all considered flight conditions. Hence, the flow properties at the nozzle exit plane are independent of the surrounding flow field and the thrust nozzle flow can be treated with a separate analysis. This also enables the application of detailed reaction mechanisms to characterize potential effects of chemical freezing in the expanding nozzle flow.

In the present work, the plume characteristic and exhaust gas composition at the thrust nozzle exit were obtained by a set of separate 2D axisymmetric nozzle simulations. The flow was assumed to be in chemical non-equilibrium and detailed reaction mechanisms [20, 21] were employed. The obtained flow profiles and the exhaust gas composition were then prescribed as a Dirichlet inlet condition at the nozzle exit planes of the full computational domain of the launcher. Two fuel combinations (LOX/H2 and LOX/Kerosine) were considered. The total conditions at the nozzle entrance were obtained by equilibrium analyses [18] using combustion chamber pressures of 106.5 bar and 108 bar at oxidizer to fuel ratios of 6.7 and 2.35 for the LOX/H2 and LOX/Kerosene cases, respectively.

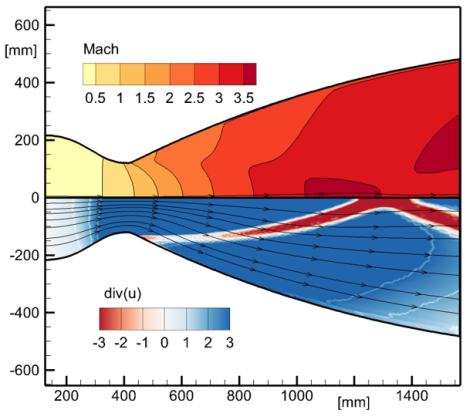

Fig. 4: LOX/H2 nozzle flow

The internal flow field for the hydrogen case is shown in figure 4. The Mach number contours show the occurrence of a internal shock which is more clearly visualized by the contours of velocity divergence in the bottom part of the figure. This shock emanates from the jump of curvature at the intersection of the nozzle throat and extension and is typical for thrust optimized nozzle setups.

The footprint of this internal flow structure is also visible in the exit profiles of flow angle, pressure, temperature and velocity which are given in figure 5. A summary of mass-flux-averaged exit conditions is given in tables 1 and 2. These values serve only for reference, the detailed profiles (as shown in figure 5) were imposed as a boundary condition in the 3D CFD investigations of the launcher. All results were obtained with a reduced 9 species - 19 step Jachimowski mechanism ([20]). Due to the fast hydrogen chemistry, they correspond to results from simple equilibrium analysis.

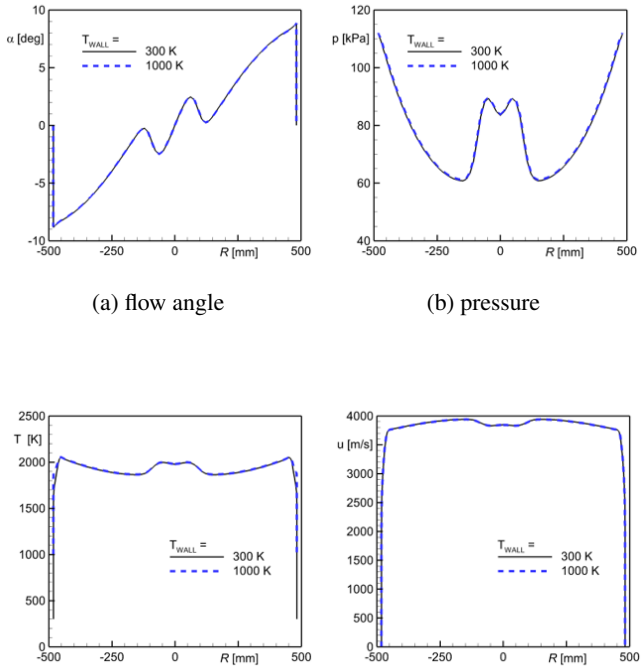

(a) flow angle (b) pressure

(c) temperature (d) velocity

Fig. 5: LOX/H2 nozzle exit profiles

Mach number contours and the axial distribution of major exhaust constituents of the LOX/Kerosene case are shown in figure 6. Here, the result of a chemical equilibrium computation is included for reference. The Mach number contours are identical for both chemical modeling assumptions, see figure 6a. Again, the internal shock is clearly visible. The axial distribution of CO2 and H2O mass fractions, depicted in figure 6b, show that the gas composition at the exit is substantially identical to the equilibrium composition. However, the impact of the internal shock can clearly be seen in the internal deviations downstream of x = 1m. The equilibrium composition follows the rapid change in local thermodynamic

properties. In contrast to that, the slower chemical kinetics of the non-equilibrium case tends to "smear out" the local shock driven disturbances of the internal flow field.

The non-equilibrium results for the LOX/Kerosene case were obtained with a detailed 19 species - 66 step high-pressure CH4 ([21]) mechanism which is a simplified variant of the GRI3.0 scheme. Again, representative mass-flux averaged exit values are included in tables 1 and 2 for reference.

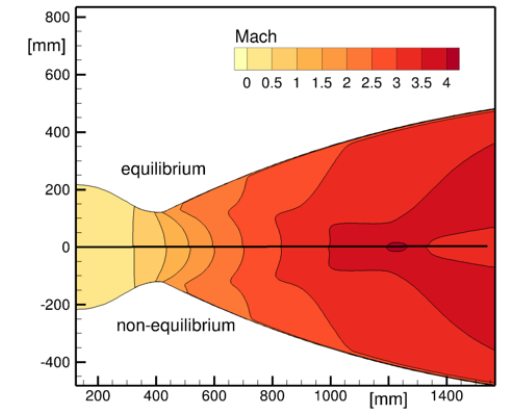

(a) flow field

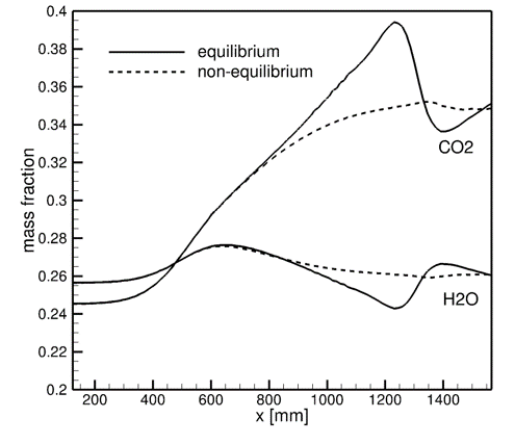

(b) centerline

Fig. 6: LOX/Kero nozzle results

6. POST-COMBUSTION EFFECTS

Due to the rich propellant mixture used in rocket engines, excess fuel is present in the exhaust plumes, which can then react with the ambient air. While it is expected, that chemical plume effects are of minor importance during ascent, the excess propellant in the exhaust jet is likely to ignite in the hot stagnation region between the plume and the free stream during retro-propulsion maneuvers. The resulting exothermal post-combustion may increase the flow temperature and, hence, the thermal surface loads. A simplified model problem was considered to identify an appropriate modeling strategy for post-combustion in the present LOX/H2 and LOX/Kerosene plumes for the large scale simulations of the RETPRO reference configuration. This model problem consists of an axisymmetric representation of a single engine being operated at the respective design conditions of H2 or Kerosene combustor. The ambient free stream represents the Mach 1.2 condition from the flight trajectory. Post-combustion was treated with a detailed-chemistry approach. For Kerosene a 19 species – 66 steps mechanism ("full") and a global Westbrook-Dryer 3 step mechanism ("simple", see [19] and table 3) were used. The hydrogen chemistry was based on a 9 species - 19 step Jachimowski mechanism [20]. The results for a chemically frozen exhaust jet is also added ("frozen"). Walls are treated with an adiabatic inviscid boundary condition.

Table 1: CFD results of the thrust nozzle exit properties

	LOX/LH2		**LOX/Kero**	
	CFD	RPA-Ref	**CFD**	RPA-Ref
$\dot{m}$ [kg/s]	215	211	271	267
U_{ax} [m/s]	3800	3883	3070	3090
p_{stat} [bar]	0.813	0.817	0.758	0.750
$T[K]$	1937	2045	1800	1806

Table 2: Gas composition at the nozzle exit plane

	H2O	H2	CO	CO2
LOX/H2	0.98	0.02	0	0
LOX/Kero	0.262	0.012	0.379	0.374

An example of the resulting temperature field and flow topology for the application of the full Kerosene scheme is shown in the top part of figure 7. A comparison of radial temperature profiles resulting from the application of different reaction mechanisms is given in the bottom part of figure 7. The location of the radial slice is indicated as a black line in the top part.

From the radial temperature distributions at $r/R_0 = 1$ (close to the rocket surface) it is visible, that for the hydrogen case, post-combustion increases the gas temperature close to the surface by about 200K. The temperature error caused by the a frozen chemistry assumption relative to the reacting case is about 14%. The impact on the surface heat load is expected to be less since the larger temperatures are associated to reduced flow densities. This result was taken as a justification to employ frozen chemistry for the 3D CFD analyses of the launcher configuration. The Kerosene case shows a more sig-

nificant impact of chemistry. Here, the increase of the gas temperature close to the surface is about 650K. This corresponds to a relative error of 40% of the frozen assumption compared to the reference case with the full chemistry. The simple 3-step global mechanism performs remarkably well with only 50K difference to the full chemistry. Based on these results, the 3D-analysis of the full launcher configuration was performed for the Kerosene case with the 3-step global mechanism.

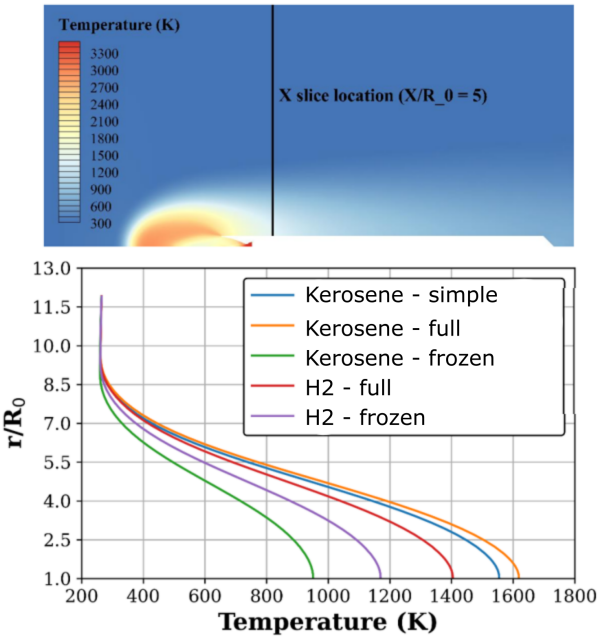

Fig. 7: Reaction mechanisms for plume-air interaction

Table 3: Modified Westbrook-Dryer mechanism, units = [m, K, mol]

Reaction	A	n	T_a
2CH4 + 3O2 = 2CO + 4H2O	5.0e11	0	24056
2CO + O2 = 2CO2	2.26e6	0	5032
backward rate	1.1e13	-0.97	39452
2H2 + O2 = 2H2O	7.9e10	0	17609
backward rate	3.48e13	0	47907

7. CFD RESULTS

In this section, the configuration characterized by 0 deg angle of attack (AoA), 0 deg thrust vector control (TVC) deflection angle and three LOX/LH2 active engines is called "baseline". A general overview of the flow-field obtained for the Mach 5.3 baseline is given in figure 8. The temperature in the x-z symmetry plane (plane of active nozzles) is shown in gray scale, surface heat flux is depicted in colors and the brown iso-surface corresponds to a threshold of 20% exhaust mass fraction. Free stream conditions are given in Tab.4.

Table 4: Free stream conditions for the Mach 5.3 baseline

Mach	$p\,[Pa]$	$u\,[m/s]$	$T\,[k]$	$\rho\,[g/m^3]$
5.3	244	1690	253	3.35

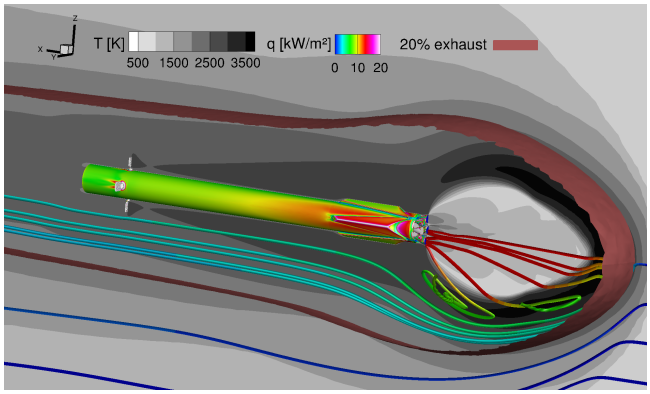

Fig. 8: Mach 5.3 baseline: Flowfield

Due to the low ambient pressure, significant post-expansion of the exhaust plume occurs. This gives rise to intense plume-plume interaction in the vicinity of the base plate which initiates localized back-flow of hot exhaust gases and associated hot spots on the base plate structure. The peak loads reach 140 kW/m². Figure 9a and 9b show details of plume-plume interactions, the formation of a stagnation zone between adjacent plumes and associated initiation of hot gas recirculation and back flow.

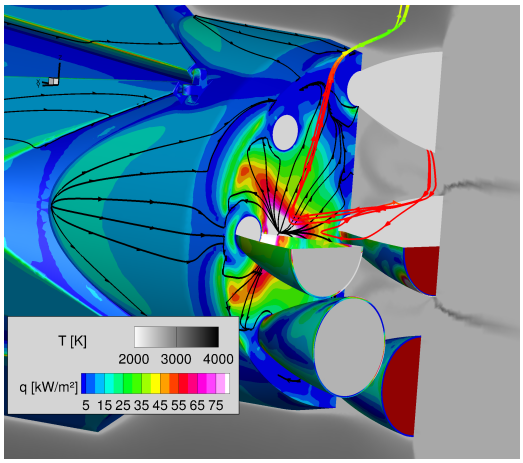

(a) flow structure

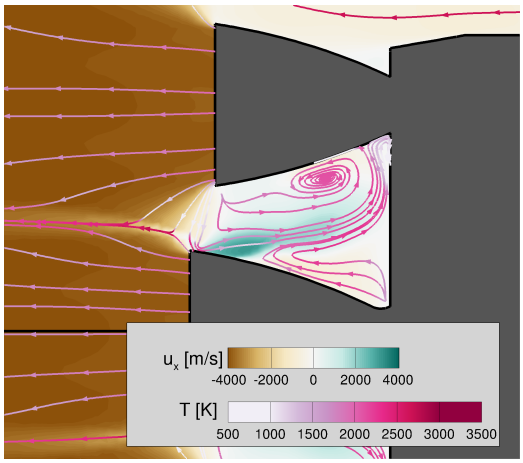

(b) planar view

Fig. 9: Mach 5.3 baseline: details in the vicinity of the base

Further upstream, the exhaust plume expands up to a Mach number of 8.2. Hence, the relative Mach number of the exhaust gases and the free stream is about 13.5. This causes a strong normal shock at the upstream end of the plume and a strong bow shock of the vehicle. The stagnation zone between those shocks is characterized by high temperatures (up to 3500K). The hot gases are then convected downstream and the entire rocket configuration is immersed in those hot exhaust products. The gas temperature close to the surface still reaches values of approximately 2000K. Nevertheless, due to the low flow densities, the surface heat fluxes on the main rocket body remain moderate with peak values around the landing leg covers of about 20 kW/m².

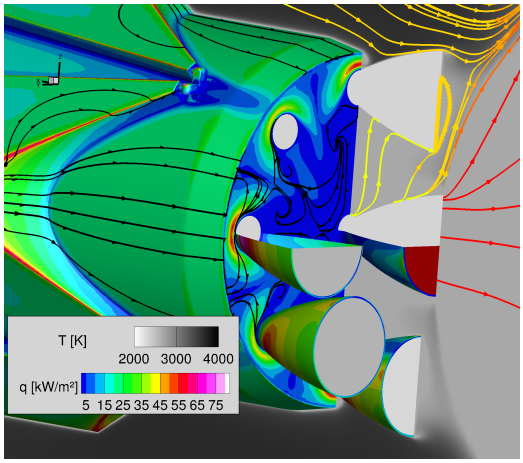

Fig. 10: Mach 5.3 single plume

Figure 10 illustrates the flow field in the vicinity of the base for only the central nozzle being active. Here, the multi-plume recirculation patterns do not occur which results in significantly reduced heat loads on the base plate. Heating occurs only at the outer edge and is driven by the impact of the reversed exhaust at the outer plume edge. The different flow patterns also visible in the skin friction lines. The heat flux peak for the multi-nozzle case is associated with an impingement topology.

The most critical components are the leading edges of the control surfaces as shown in figure 11. The leading edges of the grid fin experience local peak loads of about 350 kW/m². This value decreases very rapidly in downstream direction and occurs only at the windward surfaces of the leading edges. The sonic line (blue) indicates that the flow around the grid fins is subsonic. This is primarily a result of the slow inflow velocity of the retro-propulsion flow field and the wake of the base flow. Grid fins experience strong gradients of inflow Mach numbers and with a subsonic zone which covers about 60% of the height.

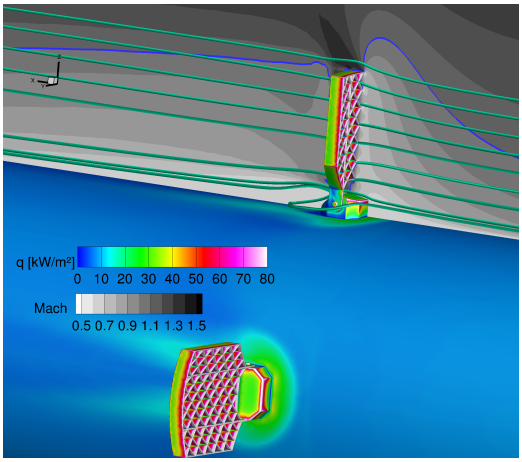

Fig. 11: Mach 5.3 baseline: grid fin heat loads

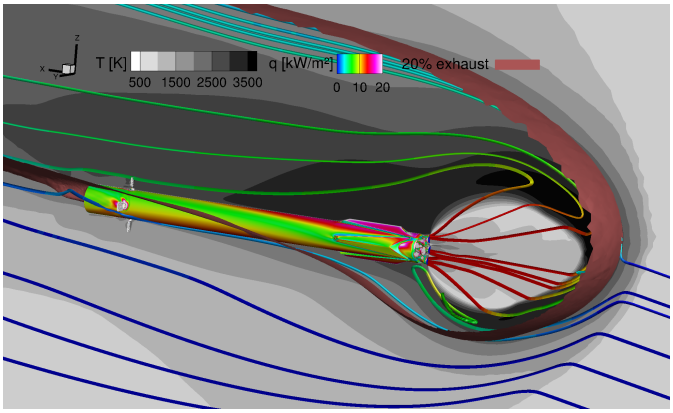

Fig. 12: Mach 5.3, AoA = 10deg: Flowfield

The introduction of 10 deg angle of attack modifies the flow field topology: the exhaust gas is deflected to the leeward side of the vehicle (see brown iso-surface in figure 12).

The windward side of the rear part of the rocket subjected to an inflow of almost uncontaminated air. Due to the high flow densities and velocities the heat loads are increased in this zone compared to the baseline case. The hot exhaust gases accumulate at the leeward side which results in a second area of increased heat loads at and around the upper landing leg cover. The near field at the base and the base heating pattern remain unaffected by the inclined inflow. The strongly under-expanded plume efficiently shields the base region from the free stream.

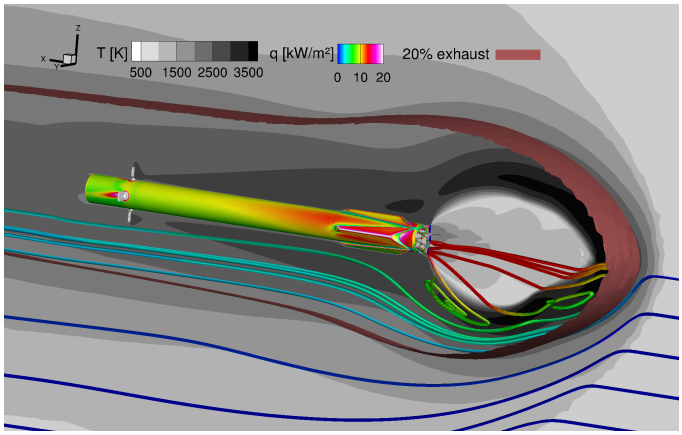

Fig. 13: Mach 5.3, TVC = 5deg: Flowfield

The effect of thrust vector control on the flow field has been also investigated. Results, shown in figure 13, highlight smaller changes in the main flow pattern. The entire vehicle is still immersed in its exhaust gases and the heat flux distribution is less asymmetric. The overall levels are comparable to the baseline case. On the other hand, the inclined central jet does alter the exhaust gas recirculation pattern near the base and the hot spot at the impingement location moves in the direction of the TVC inclination. The general flow topology remains similar as visible in the skin friction patterns, see figure 14a. Figure 14b depicts the flow structure in the symmetry plane of active nozzles.

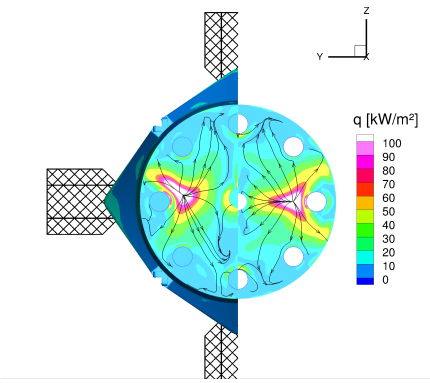

(a) Base plate heat flux

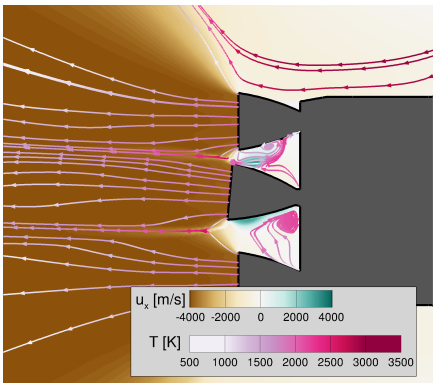

(b) Planar view of flow structure

Fig. 14: Mach 5.3, TVC = 5deg: Base flow details

The final parametric study for the Mach 5.3 flight conditions was concerned with the influence of the application of Kerosene-fueled engines and representative results are shown in figures 15 and 16. An overview of general flowfield characteristics is shown in figure 15a and 15b for frozen and reacting chemistry assumptions, respectively.

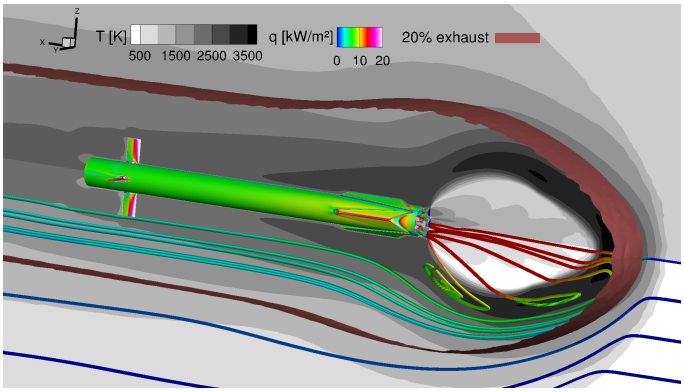

(a) frozen

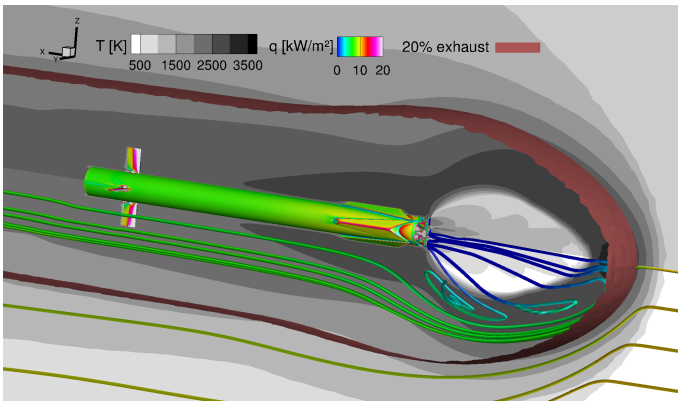

(b) reacting

Fig. 15: Mach 5.3: Kerosene fuel

The plume shape, spatial extent of the exhaust and surface heat loads are comparable to the baseline case in figure 8. Note that the flow temperature in the stagnation zone between the engine exhaust and the free stream is higher in the frozen case. In the reacting case there are endothermal reactions which dissociate exhaust species and this is due to the high stagnation temperatures and the aerothermal heating of the strong bow shock. This effect is compensated further downstream where recombination occurs and the flow temperatures in the vicinity of the rocket vehicle are comparable between the two cases.

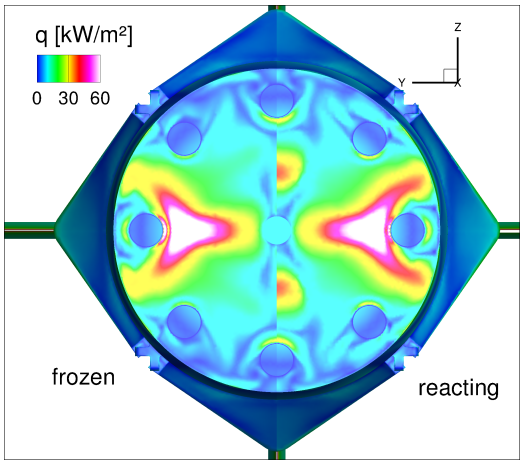

(a) Base plate

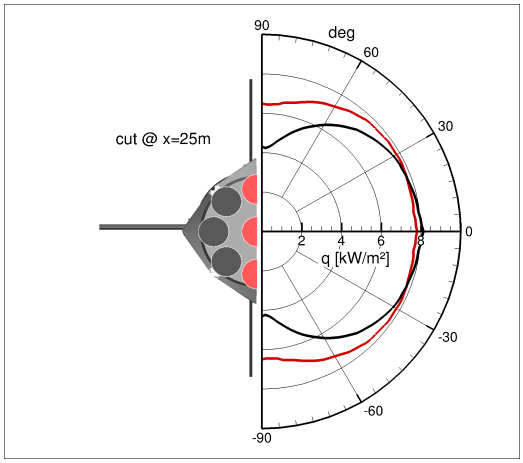

(b) Axial cut at center of the rocket

Fig. 16: Mach 5.3: Kerosene fuel: quantitative heat fluxes

The heat load distribution on the base plate is hardly influenced by post-combustion effects as visible in figure 16a. The general trend is a slight increase in the reacting case. The peak fluxes amount to about 90 kW/m² in the reacting case which is a significant reduction compared to the hydrogen fueled configuration. The surface heat flux on the cylindrical part of the rocket is influenced by post combustion only in the plane of operating nozzles as shown in figure 16b. Here, an increase is observed from about 4.2 kW/m² to 6.3 kW/m² for the reacting case. Again, the most critical components are the leading edges of the control surfaces where peak fluxes of about 400 kW/m² occur for the reacting case and 350 kW/m² in the inert results.

8. CONCLUSIONS

A comprehensive CFD study of the RETPRO flight configuration has been performed. This paper discusses representative results obtained for Mach 5.3 test case. Parametric studies include the effect of the number of operating engines, thrust vector control, and different fuels (hydrocarbon vs. hydrogen). This section summarizes characteristic and important flow features observed during the study.

Base flow:

Large plume spreading occurs due to the strong under-expansion of the nozzle flow. During the retro maneuver at the corresponding flight conditions, three engines are in operation and their plumes merge in close proximity to the base plate. This causes strong plume-plume-interactions with the formation of a stagnation zone with low axial flow momentum. This initiates strong recirculation patterns of hot exhaust gases. Hot spots on baseplate occur at the impingement location of the resulting reversed exhaust flow. The topology of these local zones of strong heating depends strongly on nozzle cluster configuration (see e.g. spatial shift for the TVC case).

Fins:

Grid fins, and more specifically their leading edges, are the components which experience the highest thermal loads. The grid fins operate in subsonic mode due to the low inflow Mach number caused by the retro-plume flow field. The separation shock upstream of the fin holder further reduces the inflow Mach number of the fins.

Rocket body:

In spite of the large flight velocity, the heat loads on the main body stay generally moderate. The reason is the strong under-expansion of the exhaust plumes which gives rise to significant post-expansion in the base region and large plume sizes. This efficiently protects the entire configuration from the incoming high speed flow. Further, the densities of the hot exhaust gases near the body are low which reduces the heat flux.

The influence of plume chemistry is noticeable for the application of hydrocarbon fuel. Due to endothermal dissociation of combustion products, the flow temperatures in the stagnation zone are slightly reduced but the recombination further downstream and the post-combustion of excess-fuel in the exhaust products locally increases the surface heat loads.

9. ACKNOWLEDGEMENTS

This project has received funding from the ESA's Future Launchers Preparatory Programme (FLPP). We gratefully acknowledge the interest in our work and the opportunity to forward this essential research.

10. REFERENCES

[1] E. Dumont, S. Stappert, T. Ecker, J. Wilken, S. Karl, S. Krummen, and M. Sippel, "Evaluation of future ariane reusable vtol booster stages," *68th International Astronautical Congress (IAC), Adelaide, Australia, 25–29 September 2017, pp. 1–18, IAC-17-D2.4.3*.

[2] S. Stappert, J. Wilken, M. Sippel, and E. Dumont, "Assessment of a european reusable vtvl booster stage," *Space Propulsion Conference, Seville, Spain, 14–18 May 2018, pp. 1–12, SP2018 00478*.

[3] A. Marwege, A. Gülhan, J. Klevanski, J. Riehmer, D. Kirchheck, S. Karl, D. Bonetti, J. Vos, M. Jevons, A. Krammer, and J. Carvalho, "Retro propulsion assisted landing technologies (retalt): Current status and outlook of the eu funded project on reusable launch vehicles," *70th International Astronautical Congress (IAC), Washington D.C., United States*, 2019.

[4] E. Dumont, T. Ecker, C. Chavagnac, L. Witte, J. Windelberg, J. Klevanski, and S. Giagkozoglou, "Callisto - reusable vtvl launcher first stage demonstrator," *Space Propulsion Conference, Seville, Spain, 14–18 May 2018, pp. 1–10, SP2018 00406*.

[5] E. Dumont, S. Ishimoto, P. Tatiossian, J. Klevanski, B. Reimann, T. Ecker, L. Witte, J. Riehmer, M. Sagliano, S. G. Vincenzino, I. Petkov, W. Rotärmel, R. Schwarz, D. Seelbinder, M. Markgraf, J. Sommer, D. Pfau, and H. Martens, "Callisto: a demonstrator for reusable launcher key technologies," *32nd International Symposium on Space Technology and Science (ISTS). Fukui, Japan, June 2019*.

[6] D. Kirchheck, A. Marwege, J. Klevanski, J. Riehmer, A. Gülhan, S. Karl, and O. Gloth, "Validation of wind tunnel test and cfd techniques for retro-propulsion (retpro): Overview on a project within the future launchers preparatory programme (flpp)," *and Re-entry Missions and Engineering (FAR), Monopoli, Italy, 2019*.

[7] M. Laureti and S. Karl, "Aerothermal databases and load predictions for retro propulsion assisted launch vehicles (retalt)," *CEAS Space Journal, https://doi.org/10.1007/s12567-021-00413-0*, 2022.

[8] J. Vos, D. Charbonnier, A. Marwege, A. Gülhan, M. Laureti, and S. Karl, "Aerodynamic investigations of a vertical landing launcher configuration by means of computational fluid dynamics and wind tunnel tests," *AIAA SCITECH 2022 Forum, https://doi.org/10.2514/6.2022-1308*, San Diego, 2022.

[9] M. Laureti, S. Karl, A. Marwege, and A. Gülhan, "Aerothermal databases and cfd based load predictions," *2nd International Conference on Flight Vehicles, Aerothermodynamics and Re-entry Missions and Engineering (FAR), Heilbronn, Germany, 2022*.

[10] M. Laureti and S. Karl, "Aerothermal analysis of the retalt2 vehicle," *EUCASS-CEAS conference, Lausanne, Switzerland, 2023*.

[11] M. Ertl and T. Ecker, "Aerodynamic and aerothermal comparison between thecal1c and cal1d geometries for the callisto vehicle," *Aerospace Europe Conference 2023 - 10th EUCASS - 9th CEAS*.

[12] Y. Feldner, M. Ertl, S. Karl, and T. Ecker, "Numerical investigation of side-effects due to fuel outflowfrom secondary nozzles in bleed engine and gas generator-cycles of a retro propulsion-assisted launch vehicle," *Aerospace Europe Conference 2023 – 10th EUCASS – 9th CEAS*.

[13] M Ertl, T. Ecker, J. Klevanski, S. Krummen, and E. Dumont, "Aerothermal analysis of plume interaction with deployed landing legs of the callisto vehicle," *9th European Conference for Aeronautics and Space Sciences*, 2022.

[14] S. Langer, S. Schwöppe, and N. Kroll, "The dlr flow solver tau—status and recent algorithmic developments," *AIAA Paper 2014-0080*, 2014.

[15] P.R Spalart and S.R Allmaras, "A one-equation turbulence model for aerodynamic flows," *AIAA Paper 1992-0439*, 1992.

[16] T. Ecker, S. Karl, E. Dumont, S. Stappert, and D. Krause, "Numerical study on the thermal loads during a supersonic rocket retropropulsion maneuver," *Journal of Spacecraft and Rockets 57(1) 131-146*, 2020.

[17] B. Bottin, "Aerothermodynamic model of an inductively-coupled plasma wind tunnel," *PhD-Thesis, University of Liege*, 1999.

[18] S. Gordon and B. J. McBride, "Computer program for calculation of complex chemical equilibrium compositions and applications," *NASA Reference Publication 1311*, 1994.

[19] L. Wang, Z. Liu, S. Chen, and Z. Zheng, "Comparison of different global combustion mechanisms under hot and diluted oxidation conditions," *Combustion Science and Technology, 184(2):259-276*, 2012.

[20] P. Gerlinger, "An implicit multigrid method for turbulent combustion," *Journal of Computational Physics, Vol. 167: 247-276*, 2001.

[21] N.A. Slavinskaya, O.J. Haidn, and J. Steelant, "Kinetic modeling for high pressure, fuel-rich methane/oxygen combustion," .